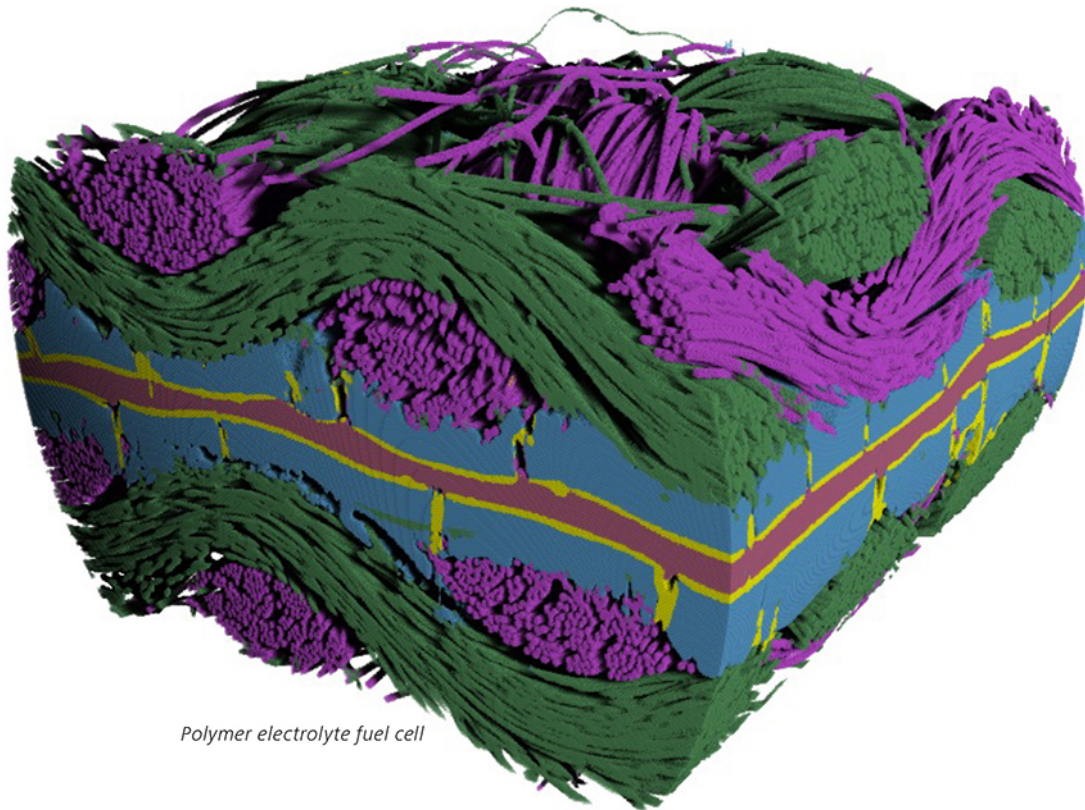


3D Characterization for Your 3D Material Structures.

- See even smaller sub-micron details
- Unprecedented image clarity at unprecedented speed enabled by AI
- UX designed for novices and experts alike



Polymer electrolyte fuel cell

Introducing ZEISS Xradia 630 Versa 3D X-ray Microscope

Seeing inside advanced materials can provide critical clues related to how structure affects performance. Achieving this insight at the microscale requires the clearest and highest-resolution 3D X-ray images. Use the newest ZEISS Xradia Versa 3D X-ray microscope (XRM) for nondestructive characterization of the finest sub-micron features within your materials. Leverage deep learning for the clearest 3D images across large representative volumes. Enjoy an intuitive, guided user experience that makes XRM technology accessible to all user skill levels.



Seeing beyond

Machine-Learning Assisted Electronic Skins Capable of Proprioception and Exteroception in Soft Robotics

Sheng Shu, Ziming Wang, Pengfei Chen, Junwen Zhong, Wei Tang,*
and Zhong Lin Wang*

Inspired by natural biological systems, soft robots have recently been developed, showing tremendous potential in real-world applications because of their intrinsic softness and deformability. The confluence of electronic skins and machine learning is extensively studied to create effective biomimetic robotic systems. Based on a differential piezoelectric matrix, this study presents a shape-sensing electronic skin (SSES) that can recognize surface conformations with minimal interference from pressing, stretching, or other surrounding stimuli. It is then integrated with soft robots to reconstruct their shape during movement, serving as a proprioceptive sense. Additionally, the robot can utilize machine learning to identify various terrains, demonstrating exteroception and pointing toward more advanced autonomous robots capable of performing real-world tasks in challenging environments.

1. Introduction

Soft robots are extensively studied as promising candidates to bridge the gap between machines and biological organisms owing to their intrinsic softness.^[1] Soft robots are usually equipped with various sensors that can provide target information from the surrounding environment to enable their effective performance. As a comprehensive platform that can accommodate multimodal sensors or even sensor arrays, e-skin technology presents a promising strategy for further augmenting the ability of soft robots. However, current progress

in e-skin is mainly concerned with perceiving external stimuli (exteroception), and only a few studies have focused on real-time monitoring of the shape of soft robots (proprioception).^[2] Body compliance and shape adaption enable soft robots to perform unique functions in confined spaces,^[3] conformable interactions,^[4] and walking over rough terrains for delivery.^[5] Koivikko et al. reported a curvature sensor based on screen-printed silver conductors to monitor the operating status of soft grippers.^[6] Li et al. integrated a distributed curvature sensor array with a soft manipulator to reconstruct its shape.^[7] Despite the accuracy of shape sensing in these studies, additional sensors that can per-

ceive external stimuli are still necessary for these soft robots in practical applications. Therefore, an e-skin that can reconstruct the shape and simultaneously react to the surrounding environment is highly desired for diversifying the capabilities of soft robots with a simplified structure.^[8]

In addition to e-skins, progress in machine learning (ML) techniques has provided abundant opportunities for developing more advanced soft robots. The combination of e-skin and ML techniques allows soft robots to perform a given task in a more intelligent manner, and the results are often beyond our expectations. For instance, Tao et al. employed convolutional neural networks to learn the deformations of a soft gripper for real-time object classification.^[9] Meerbeek et al. implemented a neuro-inspired hyperdimensional computing algorithm for the real-time gesture estimation of soft robots.^[10] Schlagenhauf et al. exploited reinforcement learning to achieve dynamic manipulation of soft robot hands.^[11] The outstanding performance of ML in exploiting datasets is suitable for analyzing sensing signals, especially in sensor arrays, which are usually characterized by the generation of numerous data in a small period. Even small differences in signals that are often neglected by humans can be precisely discerned by ML. Therefore, the combination of machine learning and shape-sensing e-skins is expected to enable the development of soft robots with advanced artificial intelligence, eventually resulting in artificial systems that can rival the abilities of biological organisms.


This study proposes a shape-sensing electronic skin (SSES) based on a differential piezoelectric matrix that can arm soft robots with both proprioception and exteroception abilities by integrating machine learning techniques. Each building block of the SSES contains a conductive fabric sandwiched between two polyvinylidene fluoride (PVDF) membranes. The outputs

S. Shu, Z. Wang, P. Chen, W. Tang, Z. L. Wang
CAS Center for Excellence in Nanoscience
Beijing Key Laboratory of Micro-nano Energy and Sensor
Beijing Institute of Nanoenergy and Nanosystems
Chinese Academy of Sciences
Beijing 100083, P. R. China
E-mail: tangwei@binn.cas.cn; zhong.wang@mse.gatech.edu

S. Shu, Z. Wang, P. Chen, W. Tang
School of Nanoscience and Technology
University of Chinese Academy of Sciences
Beijing 100049, P. R. China

J. Zhong
Department of Electromechanical Engineering
Centre for Artificial Intelligence and Robotics University of Macau
Macao 999078, China

Z. L. Wang
Georgia Institute of Technology
Atlanta, GA 30332-0245, USA

 The ORCID identification number(s) for the author(s) of this article can be found under <https://doi.org/10.1002/adma.202211385>.

DOI: 10.1002/adma.202211385

of these two PVDF membranes are identical when pressing or stretching is inflicted. Therefore, these interferences can be easily discerned and minimized using a differential strategy, resulting in satisfactory robustness for sensing bending. Proprioception is enabled for soft robots, as demonstrated by the reconstruction of surface conformations during crawling using data collected by the SSES. The precision reaches 0.0025° , and the response time is 36 ms, which is compatible with the majority of the application scenarios of soft robots.^[12] Furthermore, based on the acquired variations in shape, this study establishes a dynamic model, which can further deduce the crawling distance, gesture, and velocity for modulation and calibration. Exteroceptive ability is realized when a machine-learning strategy is introduced to analyze the SSES-acquired data. For instance, soft robots can identify various terrains or barriers, thus exhibiting advanced artificial intelligence. We expect that the SSES and its combination with machine learning techniques can provide a general approach for augmenting and diversifying the ability of soft robots to thrive in real-world applications.

2. Results and Discussion

2.1. Configuration and Characterization of SSES

Figure 1a presents an explosive illustration of the sandwiched structure of the SSES and a 3D schematic of its integration with a typical soft-crawl robot. The enlarged inset depicts the layered structure of the building blocks of the SSES, which exhibits mirror symmetry with respect to the layer of the conductive fabric (polyester cloth, 110 μm in thickness). This layer also serves as a common ground electrode, and two piezoelectric sensing units are placed on both sides. Each unit consists of a PVDF (thickness of 28 μm , polarized along the thickness) film sandwiched between two Ag electrodes, and the entire device is packaged by the outermost silicon layers. The robustness of the SSES is elaborated using a cross-sectional view of a building block, as shown in **Figure 1b**. The conductive fabric is significantly thicker than the adjacent PVDF films; therefore, the neutral layer, a non-strained layer upon bending, is located within the conductive fabric, as indicated by the red dashed line. Hence, strains produced on the two PVDF films (PVDF A and B) are expected to be opposite when the building block is bent, and identical when subjected to pressing or stretching; these are the two common influences during bending sensing.^[13] This assumption is verified by the measured outputs shown in **Figure 1c–e**; details of the measurement are available in Note S1 (Supporting Information). The building block is bent to form a convex curvature with an angle of 150° , and the acquired waveforms shown in **Figure 1c** are similar in magnitude but opposite in polarity; this is consistent with the simulated results shown in **Figure S1** (Supporting Information). However, the outputs of the two PVDF films are almost identical when the building block is stretched or pressed, as shown in **Figure 1d,e**, and **Figure S2** (Supporting Information). This feature inspired us to employ a differential approach to minimize interferences during sensing.

This approach is effective even in more complex situations, where bending is inflicted during stretching or pressing. As shown in **Figure 1f**, the outputs of PVDF A and B exhibit the same tendency when a stretching force is applied, and a pair of reversed peaks is generated when bending is inflicted. Similar profiles are observed in the case of pre-pressing, as shown in **Figure S3** (Supporting Information). Although the stretching/pressing force causes a certain shift in the neutral layer, the differential values remain nearly the same, as illustrated in **Figure S4** (Supporting Information). A theoretical analysis of the output performance is presented in Note S2 (Supporting Information). Another salient merit of the sandwiched structure is the apparent improvement in the magnitude of its signals. As demonstrated in **Figure S5** (Supporting Information), a 14-time higher peak-to-peak value is delivered when compared to that of a single-layer structure (7 V vs 0.5 V). This enhancement may be because the conductive fabric serves as an approximate translational layer (see Note S4, Supporting Information).

The linearity of the output signals is examined in **Figure 1g**, indicating a linear relationship with $R^2 = 0.9953$ for angles ranging from 24.6° to 172.8° . Meanwhile, the sensitivity is calculated to be 0.146 V deg^{-1} ,^[14] laying the foundation for high-resolution applications of SSES in robotics and healthcare fields.^[15] **Figure S6** (Supporting Information) shows that the limiting resolution of the SSES can reach 0.0025° , and it can be further enhanced by employing a more sensitive signal acquisition system or developing materials with higher piezoelectric properties. The SSES also demonstrates a fast response feature (36 ms), long cycle stability, and satisfactory robustness to other common influences, as plotted in **Figure S7** (Supporting Information). These merits of the SSES ensure its broad applications in soft robotics.

2.2. SSES Fabrication and Shape Reconstruction

The perception of surface conformations plays an essential role in acquiring the real-time operating status of soft robots, thereby providing opportunities for establishing reliable control systems to realize realistic applications. **Figure 2a** and **Figure S8** (Supporting Information) illustrate a facile strategy for building an SSES-integrated soft robot. PVDF is selected to fabricate the SSES because it can directly convert mechanical agitation into electrical output. The main body of the SSES was fabricated by laser cutting and magnetron sputtering, and the corresponding electrical connections were processed using mature printed circuit board (PCB) technology. The ultrathin thickness ($<200 \mu\text{m}$) and flexibility enable the conformal and compact assembly of SSES in soft robots. Further, serpentine electric wires in addition to island-structured PVDF films form an “island bridge”, an electrically conductive network that provides a certain stretchability for SSES.

Figure 2b shows a scheme for reconstructing a curved surface using the SSES-collected data. Specifically, an SSES array was first integrated on the target surface, and curvatures at given spots were detected by the building blocks of the array. All these local curvatures were analyzed and processed using computers to restore the conformation. Here, we consider a typical soft crawl robot, 170 mm in length and 80 mm in width,

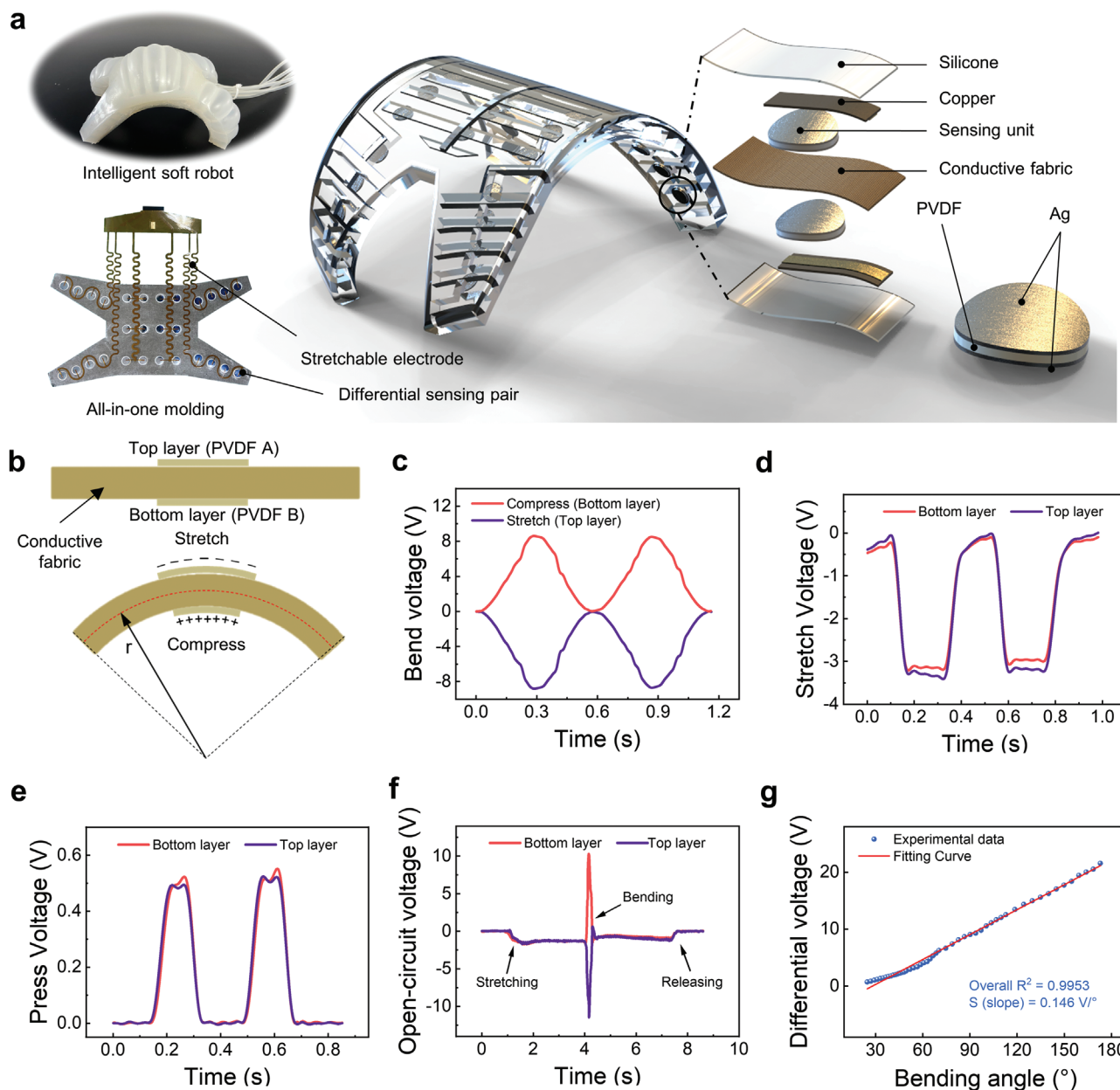


Figure 1. Configuration and characterization of SSES. a) Illustration of the SSES-mediated soft robot assembly. b) Illustration of a sensing block under bending. c) Open-circuit voltage output of the two units when bending under an angle of 150°. d,e) Output performance under stretching (0.2 mm) (d) and pressing (6.6 N) (e). f) Voltage output under bending simultaneously with stretching. g) Linear relationship between measured angles and voltage output, ranging from 24.6° to 172.8°.

as an example. The size of each block, a key parameter of the SSES, was optimized to 2.5 mm to achieve a balance between signal magnitude and spatial density (see Figure S9a, Supporting Information). Thus, 28 blocks in total were integrated into the SSES to reconstruct its overall shape; details can be found in Figure S9b (Supporting Information). As each block consists of two sensing units, a LabVIEW-based multichannel synchronous data-acquisition system was developed to simultaneously acquire 56 sets of sensing signals. These 56 sets of voltage signals were converted to corresponding curvatures and displayed on a monitor using software developed based on Unity (Figure S10, Supporting Information). With this strategy,

a close similarity was observed between the deformed soft robot and the corresponding reconstructed shape, as shown in Figure 2c and Movie S1 (Supporting Information).

In addition to the recovery of static surfaces, we also demonstrated the reconstruction of dynamic surfaces using an SSES. An Arduino-based gas control program was developed to enable the programmable bending of the soft robot's legs for crawling. Real-time bending angles at the four specified spots (Figure S9e, Supporting Information) on the feet could be acquired by the SSES, as shown in Figure 2d. The crawling process and the reconstructed version are demonstrated in Movie S2 (Supporting Information). Note S5 (Supporting Information) further

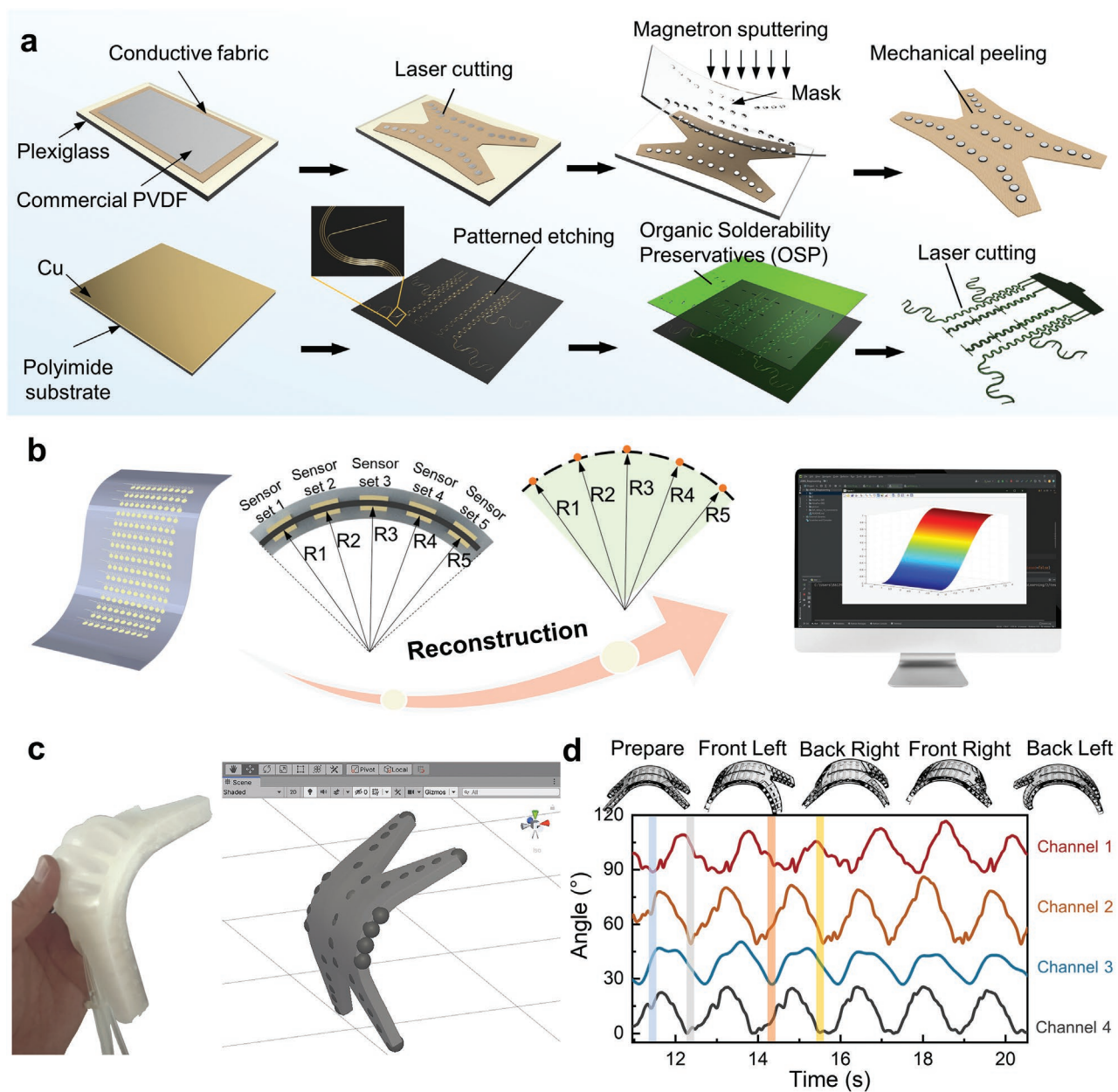


Figure 2. SSES fabrication and shape reconstruction. a) Craft flow diagram of the SSES. The laser cutting, magnetron sputtering, and organic solderability preservatives (OSP) technology facilitate the batch fabrication of SSES, and the flexible printed circuit boards increase the reliability of sensory array interconnection. b) Schematic of the reconstruction based on the sensor array. c) Computational reconstruction of the soft robot's bending. d) Measured angle curves of four sensing blocks during typical crawling motions of a soft robot. Different colors are highlighted to mark phases.

establishes a kinetic model based on the SSES-acquired signals, and various dynamic parameters, such as crawling velocity and distance, can be deduced. Hence, not only the perception of surface conformation but also the awareness of dynamic features is realized for soft robots owing to SSES integration.

2.3. Dynamic Behavior of the Robot on Various Terrain Surfaces Revealed by SSES

The variation in the bending status of the soft robot's limbs not only introduces a change in conformation but also indicates

their physical interactions with the ambient environment. This encouraged us to perceive the surrounding environment through the data collected by SSES. **Figure 3a** shows a sketch of a soft robot crawling over several representative terrains. These terrains can be discerned by the surface roughness, which is normally related to the friction coefficient. Figure S11 (Supporting Information) depicts the measured normal force and friction coefficients when the soft robot crawls on these terrains; further details can be found in Note S6 (Supporting Information).

The flow diagram in Figure 3b illustrates the principle of identifying different terrains via the statistical analysis of the

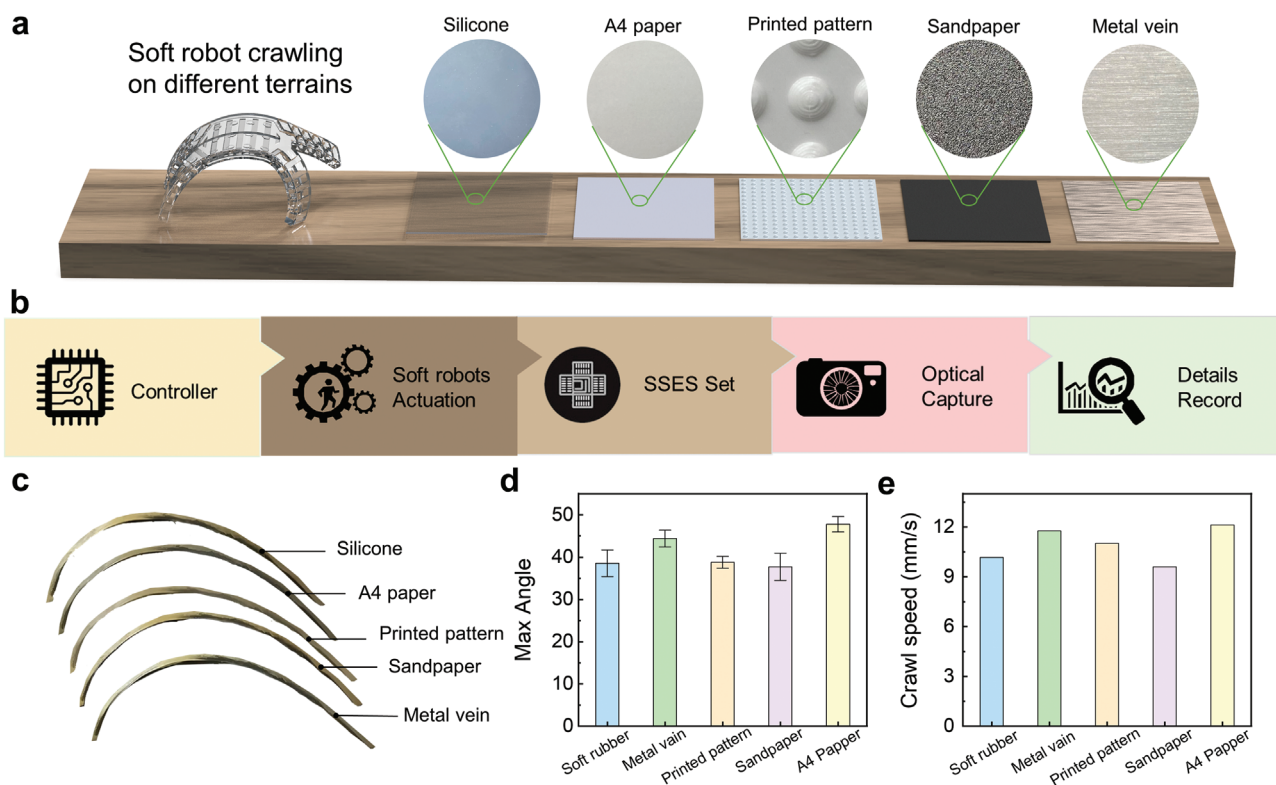


Figure 3. Dynamic moving behavior analysis of a soft robot crawling on various terrain surfaces. a) Schematic of the soft robot crawling over various terrains. The enlarged views are optical images of different terrain surfaces. b) Flow diagram for verifying the feasibility of sensing ambient environment based on SSES-acquired data. c) Outlines of the bottom surface of the soft robot when it crawls over various terrains. d) The mean maximum bending angle at the spot of the robot's left forefoot, measured by SSES over 10 trials. Error bar denotes standard error of the mean. e) Average crawling speed of the soft robot when it crawls over different terrains.

SSES-acquired data. First, the SSES-integrated soft robot was made to crawl over five different terrains (Figure S12, Supporting Information), and its gestures during crawling were simultaneously captured by a high-frame camera. Subsequently, the SSES-collected signals were statistically analyzed and compared with the differences in the optical images. Although the five outlines of soft robots during crawling exhibit an overall similar shape, as shown in Figure 3c and Figure S13 (Supporting Information), significantly small angular differences in the four limbs existed during crawling, as revealed by the frame-by-frame optical images, as shown in Figure S14a (Supporting Information), and the detected data from the attached commercial inclination sensors, as shown in Figure S14b (Supporting Information). This can be explained by the fact that the larger the surface roughness, the higher the friction that resists the bending deformation of the robot, and a smaller maximum bending angle (MBA) is expected (Figure S14c, Supporting Information).

To verify this assumption, the maximum bending angles during crawling were extracted from the SSES-acquired data after the statistical analysis. As shown in Figure 3d, the A4 paper, which had the lowest roughness among the five terrains, resulted in the highest MBA of the soft robot. In contrast, sandpaper or soft rubber, which demonstrated larger roughness, resulted in a smaller MBA during crawling. Furthermore, this phenomenon is supported by the differences in crawling speed, as shown in Figure 3e, in which the fastest crawling speed is

obtained on A4 paper, whereas the speed on soft rubber or sandpaper is considerably slower. These detailed differences during the crawling process enable us to develop a rapid and reliable strategy based on the SSES to identify different terrains.

2.4. Environment Awareness of SSES-Integrated Soft Crawling Robot

Analysis based on reconstructed conformation usually relies on complicated image processing techniques, and the interaction between soft robots and their surrounding environment can be statistically reflected by SSES-measured data. Thus, we attempted to employ machine learning (ML) technology to further exploit SSES-acquired data to realize environmental awareness. To establish an optimal ML training model, efforts have been made to examine the appropriate feature extraction method and optimized algorithm (Figures S15–S17 and Table S1, Supporting Information). The node-oriented decision tree algorithm was preferred because the signals were interleaved, and this method enabled us to build multiple decision trees and consider the average to fully exploit the advantages of various models. Moreover, the fact that only sensing units at certain specific spots exhibit pronounced responses is expected to maximize the benefits of node classification.^[16] The processing procedure is shown in Figure 4a. The features were extracted before the analysis. Voltage signals instead of derived angles

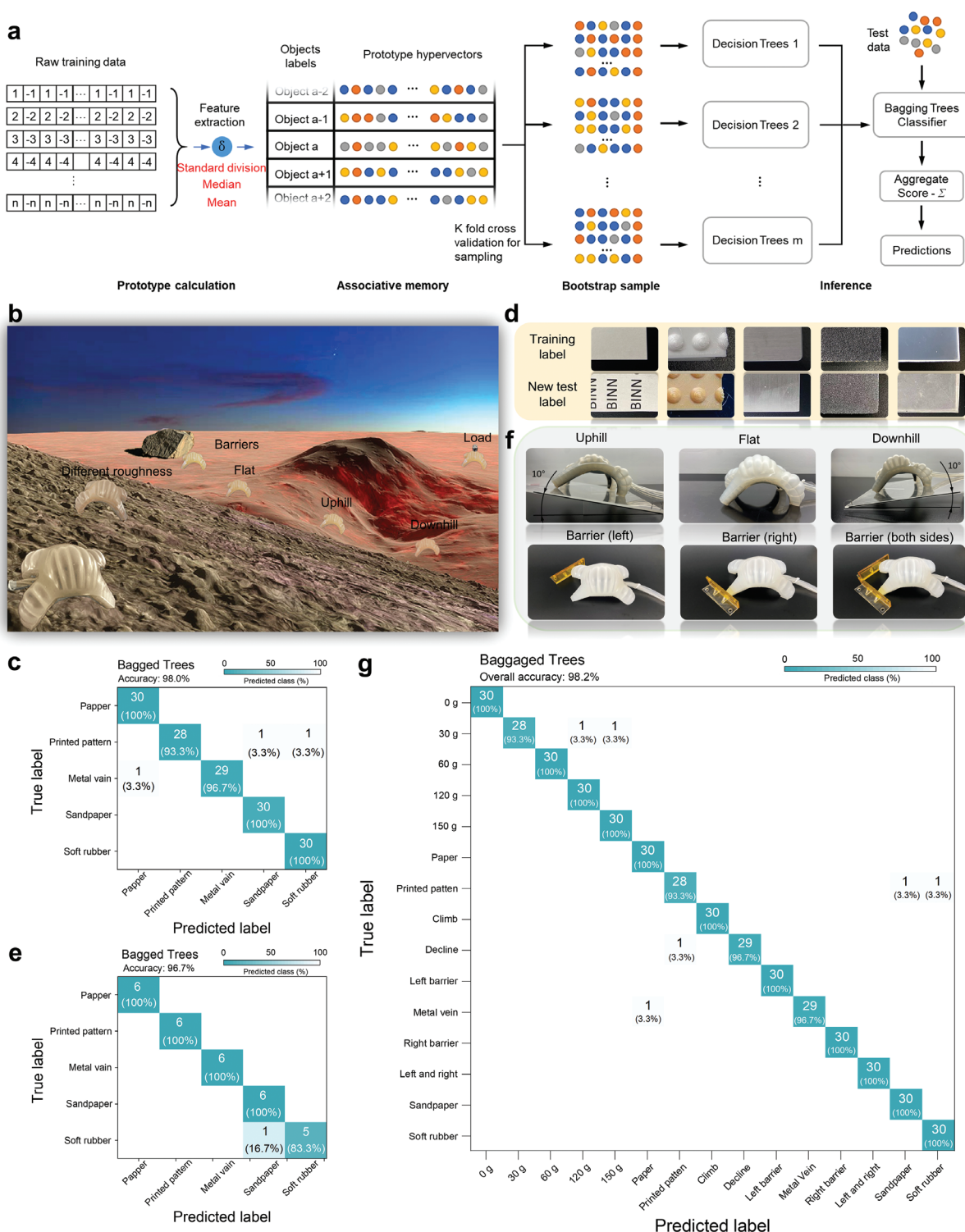


Figure 4. Environment awareness of SSES-integrated soft crawling robot. a) Flow diagram of the machine learning process. The bagged tree algorithm is chosen. b) Conceptual illustration of the soft robot for environment recognition. c,d) Optical images of the experiment scenarios. e) Terrain surface training with five-fold cross-validation (five different trained pavements with varying roughness). f) Identification of five new terrains that have not been trained to demonstrate the generalization ability of the developed model. The new A4 paper is printed with ink; the new printed pattern is printed with smaller embossment and different materials; the new metal is slightly polished; the new sandpaper's grit size is 20% smaller (from 80# mesh to 100# mesh); the new soft rubber is contaminated with dust. g) Mixed recognition of all the aforementioned environments, with an overall accuracy of 98.2%.

were employed as raw data because more information was contained in the directly measured signals, which is beneficial for improving the accuracy of ML analysis. The standard deviation, median, and mean of the raw data were extracted as features. After classification, these features were packaged into several decision tree algorithms for training, and the results of the five-fold cross-validation and new datasets test were obtained.

Figure 4b depicts the expected conceptual illustration of an SSES-integrated soft robot for environment recognition after its confluence with the ML technique. Figure S18 (Supporting Information) shows the classification results of different grit sizes of sandpapers, indicating that roughness is the only indicator of identification. Figure 4c shows that five terrains with different roughness values can be identified by a series of statistical data combined with ML with a high accuracy of 98.0%, indicating the feasibility of the developed model. To examine the generalization ability of this model, the modified terrains (Figure 4d; Figure S19, Supporting Information) were added to the prediction set: the new A4 paper is printed with ink, which actually decreases the surface roughness owing to the presence of carbon; the printed pattern is modified with smaller patterns and different materials; the new metal is slightly polished; the grit size of the new sandpaper is reduced from 80# mesh to 100# mesh; the new soft rubber is covered with dust. The integration of ML analysis with the SSES-armed robot results in a satisfactory identification accuracy of 96.7% (Figure 4e).

Similar to the roughness of terrains, different weight loads, inclinations, and obstacles induce corresponding variations in sensing signals, implying that identifying these parameters using ML is feasible. The training scenarios and real-time variations in the signals are shown in Figure 4f and Movie S3 (Supporting Information). Here, fivefold cross-validation was conducted, using four sets of data for training and one set for testing. Further details can be found in Experimental Section. After training, a road with a slope of 10° in either the uphill or downhill directions could be recognized with an accuracy of 97.8% (Figure S20a, Supporting Information), the positions of barriers on the road could be discerned (Figure S20b, Supporting Information), and the weights of the carried items could be recognized (Figure S20c, Supporting Information).

Furthermore, to explore the comprehensive perception of the environment, we mixed all 20 terrain/barrier/load conditions in the identification test (Figure S21 and Table S2, Supporting Information). The results show an overall accuracy of 98.2%, as shown in Figure 4g. It is noteworthy that although the employed decision tree algorithm is credited with a certain degree of generalization, the accuracy is unsatisfactory when this model is confronted with some out-of-distribution problems, especially for those involving multiple sensations simultaneously. This deficiency is attributed to the vulnerability of the decision tree algorithm. The use of deep neural networks or increasing data richness to obtain more information on the environment is expected to further improve this model.

3. Conclusion

A shape-sensing electronic skin (SSES) was developed to sense the dynamic status of soft robots during operation. The limiting

resolution was 0.0025° , and the external interferences were minimized owing to the differential piezoelectric matrix with a coplanar mirror sandwiched structure. This study proposed two processing principles regarding SSES-measured data. Specifically, we first developed a general strategy for reconstructing the surface conformations of soft robots according to SSES-obtained data, thus enabling the proprioceptive abilities of soft robots. In addition, we introduced machine learning (ML) technology to analyze SSES-generated data for identifying different terrains, loading weights, and obstacles, thus endowing soft robots with exteroceptive abilities and primary intelligence. SSES and its integration with ML techniques lay the foundation for soft robots to effectively acquire their own status and interact with the environment in a sophisticated manner. We expect that this paradigm will inspire more innovations that allow soft robots to swiftly cope with challenges in real-world applications.

4. Experimental Section

Shape-Sensing Electronic Skin (SSES) Fabrication: The SSES was composed of two pieces of piezoelectric film (polyvinylidene difluoride, PVDF, $28\ \mu\text{m}$ in thickness, MEAS) with silver electrodes (Epoxy conductive adhesive, $6\ \mu\text{m}$ in thickness, LX-30 Yinxi) on both sides, a thin flexible conductive fabric (Polyester cloth, $110\ \mu\text{m}$ in thickness, Ebenda 8869) with glue on both sides, a pair of flexible printed board ($100\ \mu\text{m}$ in thickness), and a thin layer of silicone ($\approx 1\ \text{mm}$ in thickness, Eco-flex 0030, Smooth-On) encapsulation. The fabrication of the sensor pair began by preparing two films of PVDF with silk screen printed silver glue on one side. Then the two PVDF films (the sides with silver glue) were symmetrically pasted on both sides of the double-sided adhesive conductive fabric ($110\ \mu\text{m}$ in thickness, Ben Yida). The size of the conductive fabric was larger than the PVDF film, which facilitated subsequent fixation. Then flatly affix the raw sandwich structure on a Plexiglas substrate ($2\ \text{mm}$ in thickness, Creromem) of appropriate size that was cleaned with alcohol, removed air bubbles. After that, three steps of laser cutting were required. First, the upper layer of PVDF was cut using the laser-cutting machine (PLS6. 75) with appropriate focal length ($2\ \text{mm}$), power (18%), and cutting speed (70%), which required dot positioning through the designed pattern. Second, flip to the other side was flipped and the previous dots were used to position the new face, and the laser parameter was the same as last step. Third, having prepared the sensing matrix, the same method was used to define boundaries (focal length ($2\ \text{mm}$), power (80%), and cutting speed (50%)). As can be seen, accurate positioning is very important, especially for the first time, which usually requires multiple points of repeated positioning. Afterward, a single fluorinated polyethylene terephthalate (PET) film ($50\ \mu\text{m}$ in thickness) mask, whose pattern was slightly smaller than that of the PVDF sheets and defined by laser cutting, was placed on the patterned PVDF film, fixing by previous adhesive conductive fabric. The whole surface was kept clean and electroplate it with magnetron sputtering apparatus (Cr/Ag, $10\ \text{nm}/100\ \text{nm}$ in thickness). Finally, in an alcohol environment, mechanically peeled off the defined structure from the Plexiglas substrate. Here, PVDF is superior to other piezoelectric material because PVDF is a polymer with lower thermal conductivity than other piezoelectric materials, which increases the precision of laser processing by allowing heat to be concentrated more easily.^[17]

As for the connecting wire, a soft, thin polyimide film covered with copper ($80\ \mu\text{m}$ in thickness in total) is employed as a substrate, and the serpentine patterned design enables its flexibility and stretchability, meeting the tiny displacement when it bends. On the polyimide substrate, copper wires with width of $0.15\ \text{mm}$ and spacing of $0.1\ \text{mm}$ are etched as the electrodes (Figure S2, Supporting Information). The width and spacing of the electrode lines on the inside are consistent,

so that the interconnection electromagnetic interference is minimized. The resistance difference caused by the change in the length of the outer side is also consistent by appropriately modifying the line width and height. Organic Solderability Preservatives (OSP) technology was used to selectively overlay printed circuit board, so that the signal could be well exported. The flexible electrode board is only 0.1 mm thick and can be well attached to the conductive cloth substrate without affecting its bending. Besides, the areas where the board contacts the sensors are only 0.45 mm², which is much smaller than the area of the sensors themselves, so as to further reduce the influence of the electrode wires on bending and ensures the output consistency.

The packaging of the SSES was carried out in the printed mold. The 1:1 (Eco-flex A: B) mixed eco-flex was spread on the bottom of the mold, and then it was put into the sensor array, and then the mold was filled with eco-flex and the bubble was removed with pointed tweezers, waiting for 2 h at room temperature, and it was mechanically peeled off from the mold.

Soft Gripper and Robot Fabrication: The soft four-jaw gripper is made of Eco-flex (0030, Smooth-on), nylon wires (Fashion Fish), rubber hose (2 mm in inner diameter, Takuhiro), and silicone adhesive (Smooth-on Sil-Poxy). Eco-flex A and B was mixed in a same ratio, stirred evenly, and placed in a 3D-printed mold. A vacuum pump (Pritchett AP-01P) was employed to remove bubbles. After 2 h of resting at room temperature, gripper was removed from the mold and nylon wire was wrapped around it. Then a thin layer of eco-flex was applied to the gripper wrapped in nylon wire. The preparation method of the soft crawl robot body is basically the same as that of gripper, yet nylon wire's is unnecessary. The fabrication of the software robot has already been reported, and here is a focus on the process of bonding with the sensor array. Similarly, a thin layer of eco-flex is applied to the bottom of the SSES, then the soft body is placed in the appropriate position, the edges are further sealed with eco-flex, and settled to cure. Once cured, the rubber hoses, which use silicone adhesive to seal with the soft body, are used for connecting Arduino-controlled Solenoid valves and pumps.

Data Acquisition and Processing: The voltage output collection of the SSES was accomplished mainly by voltage preamplifier (Keithley 6517 System Electrometer). And only in the data acquisition process for ML is the multi-channel data acquisition system (National Instrument 4300, internal resistance is ≈140 MΩ) applied. Here, the customized interactive control software programmed by LabVIEW completes the analog-to-digital conversion and records the data. When studying the characteristics of a single pair, the signal is generated by the patch in series between the linear motor (Linmot, E1100). Also, an ultra-high precision manual linear slide (NFP-x462, Zolix) is employed for accuracy calibration. The whole measurement process of the system was fixed on the optical platform. Moreover, the mechanical measurement of the sensor pair was done by a high-precision commercial force sensor (Oruda, AT8301), and the mechanical data were directly read and stored by its matching software.

The soft crawling robot dynamical system is composed of four parts: pump (Jie Dong SP-36-9), solenoid valve group (Airtac 025-06), controller (Arduino), and amplifier. The pump provides stable air pressure and leads to the solenoid valve group via a rubber hose, the sequence switch of the solenoid valve group is controlled by an external amplifier of the Arduino controller, and the outlet of the solenoid valve is connected to the soft robot porosity. The airtightness of the rubber hose is guaranteed by a silicone adhesive.

In the recognition with ML, the data were directly collected and recorded by the multi-channel data acquisition system and the corresponding LabVIEW program, and further processed by Origin to reduce data dimensions and extract the characteristic data. The learning algorithm was provided by the MATLAB toolbox. The standard deviation of the 50 signals of the gripper and the 56 signals of the crawling robot as a set of data were designed. More specifically, the multi-channel data were imported into Origin, and Origin's mathematical statistics were used to calculate a series of parameters such as standard deviation, variance, and mean, and the feasibility of these data after dimensionality reduction was compared to the corresponding algorithm. Meanwhile, fivefold cross-validation was conducted here. To make the data of

input lists to be more comprehensive, two more features, the mean and median, were extracted from the raw data, and learning the three kinds of feature data simultaneously could increase the final recognition accuracy by 1.5% (Figure 4g). After training and prediction, the results were further imported into origin for normalization, visualization, etc. During the experiment for terrains recognition, all these tested surfaces were tightly adhered to a desktop while no visible move, wrinkle, or bulge would be produced when the soft robot was crawling on. Besides, the thin thickness of these substrates (0.1-3 mm) could further reduce the influence from compliance.³¹ Hence, interferences from surface compliance are supposed to be very limited in surface roughness experiments. As for the adhesion resulted from chemical properties, silicone rubbers, such as eco-flex and PDMS, are mainly consists of SiO₂ which is chemically inert to a majority of chemicals in ambient conditions. And no chemical interactions have been reported among silicon rubber and five surfaces employed in our experiment. Thus, the influence caused by chemical adhesion could be reasonably excluded.

The reconstruction of soft crawling robots is validated by reconstruction system based on Unity and data acquisition system based on LabVIEW. We designed and encode a new LabVIEW program that allows voltage information to be read directly from data acquisition cards (National Instrument 6356), and through the collaboration of multiple collection cards, we have achieved data acquisition of arrays. The collected data is read by the Unity program (Version 2019.4.25f1c1), and after simple data processing such as filtering, differential, and proportional conversion, the voltage signal is converted into an angle value, which gives dynamic changes to the joints of the model in Unity. It is worth noting that the joint bending system is based on a relative coordinate system, and the movement of the limbs near the main body is implicated.

Statistical Analysis: All raw statistical data were collected by NI acquisition cards in conjunction with the LabView program, as described in Experimental Section 4.3. In the feature extraction process, the mean, standard deviation, median, and maximum values are obtained by entering the original data into Origin and obtaining the corresponding statistics data with its statistical module. In the image recognition feature extraction procedure, Origin is used to produce the waveform graph, and then the MATLAB program extracts the image gray difference statistics, including mean, contrast, and image entropy. Additionally, Origin is used in the heat map to normalize the data from multiple channels in order to enable the observation of the rules between different types of data. Other simple data processing tasks, such as differentiation, angle conversion, filtering, and so on, are handled by the Origin toolkit. Moreover, all error bars are presented in mean ± SD, and 10 points from each set of data are taken to calculate the mean and standard deviation. When conducting the recognition with the gripper, each object is grasped ≈50 times. And except for objects such as blades and bananas, which can only be grasped from a fixed direction, the direction of each grasp is random and changeable, so that the total data set (containing 43 500 sets) is obtained. In environment recognizing, the total data (containing 25 125 sets) are acquired through crawling on objects 30 times (Among them, the zero-weight and flat-road group are the same data). The training and testing datasets for objects and environment recognition are randomly selected from the total dataset.

Supporting Information

Supporting Information is available from the Wiley Online Library or from the author.

Acknowledgements

The research was supported by the National Key R&D Project from the Minister of Science and Technology (2021YFA1201604, 2021YFA1201601, and 2021YFA1201603); Youth Innovation Promotion Association CAS,

Beijing Municipal Science & Technology Commission (Z171100000317001, Z171100002017017, and Y3993113DF); and National Natural Science Foundation of China (grant nos. 51605033, 51432005, 5151101243, and 51561145021).

Conflict of Interest

The authors declare no conflict of interest.

Authors' Contribution

S.S. and Z.W. contributed equally to this work. W.T. and Z.L.W. conceived the idea and designed the experiment. S.S. fabricated the device. S.S., Z.W., and P.C. performed the electrical measurements. S.S., Z.W., and W.T. analyzed the data. S.S. prepared the figures. J.Z. revised the data and figures. S.S., Z.W., W.T., and Z.L.W. wrote the manuscript. All the authors discussed the results and reviewed the manuscript.

Data Availability Statement

The data that support the findings of this study are available from the corresponding author upon reasonable request.

Keywords

curvature, intelligent soft robots, machine learning, shape-sensing skin

Received: December 5, 2022

Revised: February 1, 2023

Published online:

- [1] D. Rus, M. T. Tolley, *Nature* **2015**, 521, 467.
 [2] a) G. Li, S. Liu, L. Wang, R. Zhu, *Sci. Robot.* **2020**, 5, eabc8134; b) S. Terryn, J. Brancart, D. Lefebvre, G. Van Assche, B. Vanderborght, *Sci. Robot.* **2017**, 2, aan4268; c) I. M. Van Meerbeek, C. M. De Sa, R. F. Shepherd, *Sci. Robot.* **2018**, 3, aau2489; d) B. Ying, R. Z. Chen, R. Zuo, J. Li, X. Liu, *Adv. Funct. Mater.* **2021**, 31, 2104665.
 [3] a) R. F. Shepherd, F. Ilievski, W. Choi, S. A. Morin, A. A. Stokes, A. D. Mazzeo, X. Chen, M. Wang, G. M. Whitesides, *Proc. Natl.*

- Acad. Sci. USA* **2011**, 108, 20400; b) Y. Wu, J. K. Yim, J. Liang, Z. Shao, M. Qi, J. Zhong, Z. Luo, X. Yan, M. Zhang, X. Wang, R. S. Fearing, R. J. Full, L. Lin, *Sci. Robot.* **2019**, 4, aax1594; c) X. Yang, L. Chang, N. O. Pérez-Arancibia, *Sci. Robot.* **2020**, 5, aba0015.
 [4] a) H. Lu, M. Zhang, Y. Yang, Q. Huang, T. Fukuda, Z. Wang, Y. Shen, *Nat. Commun.* **2018**, 9, 3944; b) A. Rafsanjani, Y. Zhang, B. Liu, S. M. Rubinstein, K. Bertoldi, *Sci. Robot.* **2018**, 3, aar7555; c) G. Gu, J. Zou, R. Zhao, X. Zhao, X. Zhu, *Sci. Robot.* **2018**, 3, aat2874; d) T. Jin, Z. Sun, L. Li, Q. Zhang, M. Zhu, Z. Zhang, G. Yuan, T. Chen, Y. Tian, X. Hou, C. Lee, *Nat. Commun.* **2020**, 11, 5381.
 [5] a) Y. Kim, G. A. Parada, S. Liu, X. Zhao, *Sci. Robot.* **2019**, 4, aax7326; b) C. Li, G. C. Lau, H. Yuan, A. Aggarwal, V. L. Dominguez, S. Liu, H. Sai, L. C. Palmer, N. A. Sather, T. J. Pearson, *Sci. Robot.* **2020**, 5, eabb9822; c) W. Hu, G. Z. Lum, M. Mastrangeli, M. Sitti, *Nature* **2018**, 554, 81.
 [6] A. Koivikko, E. S. Raei, M. Mosallaei, M. Mäntysalo, V. Sariola, *IEEE Sens. J.* **2017**, 18, 223.
 [7] T. Li, L. Qiu, H. Ren, *IEEE ASME Trans. Mechatron.* **2020**, 25, 406.
 [8] B. Shih, D. Shah, J. Li, T. G. Thuruthel, Y. L. Park, F. Iida, Z. Bao, R. Kramer-Bottiglio, M. T. Tolley, *Sci. Robot.* **2020**, 5, eaaz9239.
 [9] C. Larson, J. Spjut, R. Knepper, R. Shepherd, *Soft Rob.* **2019**, 6, 611.
 [10] A. Moin, A. Zhou, A. Rahimi, A. Menon, S. Benatti, G. Alexandrov, S. Tamakloe, J. Ting, N. Yamamoto, Y. Khan, F. Burghardt, L. Benini, A. C. Arias, J. M. Rabaey, *Nat. Electron.* **2021**, 4, 54.
 [11] C. Schlagenhauf, D. Bauer, K.-H. Chang, J. P. King, D. Moro, S. Coros, N. S. Pollard, presented at *2018 IEEE-RAS 18th Int. Conf. on Humanoid Robots (Humanoids)*, IEEE, Beijing, China **2018**.
 [12] a) Y. Liu, B. Chen, W. Li, L. Zu, W. Tang, Z. L. Wang, *Adv. Funct. Mater.* **2021**, 31, 2104770; b) M. S. Verma, A. Ainla, D. Yang, D. Harburg, G. M. Whitesides, *Soft Robot.* **2018**, 5, 133; c) J. Zhang, A. Jackson, N. Mentzer, R. Kramer, *Front. Robot. AI* **2017**, 4.
 [13] a) S. Timoshenko, J. M. Gere, in *Theory of Elastic Stability*, 2nd ed., McGraw-Hill, Inc, NY **1961**, pp. 107–113; b) Z. Gao, J. Zhou, Y. Gu, P. Fei, Y. Hao, G. Bao, Z. L. Wang, *J. Appl. Phys.* **2009**, 105, 113707.
 [14] Z. Zhou, K. Chen, X. Li, S. Zhang, Y. Wu, Y. Zhou, K. Meng, C. Sun, Q. He, W. Fan, E. Fan, Z. Lin, X. Tan, W. Deng, J. Yang, J. Chen, *Nat. Electron.* **2020**, 3, 571.
 [15] a) Z. Wang, J. An, J. Nie, J. Luo, J. Shao, T. Jiang, B. Chen, W. Tang, Z. L. Wang, *Adv. Mater.* **2020**, 32, 2001466; b) H. Wang, M. Totaro, L. Beccai, *Adv. Sci.* **2018**, 5, 1800541.
 [16] a) C. Kingsford, S. L. Salzberg, *Nat. Biotechnol.* **2008**, 26, 1011; b) B. Charbuty, A. Abdulazeez, *J. Appl. Sci. Technol. Trends* **2021**, 2, 20; c) S. B. Kotsiantis, *Artif. Intell. Rev.* **2011**, 39, 261.
 [17] P. Saxena, P. Shukla, *Adv. Compos. Hybrid Mater.* **2021**, 4, 8.